A Pedestrian Positioning Method for Urban Canyon Environments Using Magnetic Field Matching/Inertial Odometry Fusion

Shiyi Chen[®], Jian Kuang[®], Yan Wang[®], Tingwei Wang[®], and Xiaoji Niu[®], Member, IEEE

Abstract—In urban canyon environments, global navigation satellite systems (GNSSs) frequently fail to provide reliable positioning services due to signal obstruction and multipath effects. This article proposes a pedestrian positioning method that integrates magnetic field matching, learned inertial odometry, and an inertial navigation system (INS). Initially, the feasibility of magnetic matching positioning is validated by investigating the magnetic field characteristics in typical urban canyons. Subsequently, magnetic field profiles are constructed using relative position and attitude information generated by learned inertial odometry, rather than conventional pedestrian dead reckoning (PDR), thereby enhancing the adaptability of the magnetic matching algorithm to transition between different phone holding modes and usage scenarios. Furthermore, to address the limitation of the extended Kalman filter (EKF) in integrating historical state information, the multistate constraint Kalman filter (MSCKF) is employed to fuse INS, relative displacement increments from learned inertial odometry, and magnetic matching positioning results, thus formulating a robust and reliable pedestrian positioning solution. The proposed method is evaluated through multiple field tests in an urban canyon environment, covering an area of 5000 m² with a total walking distance of 8.25 km, achieving a positioning accuracy with a root-mean-square (rms) error of 2.98 m.

Index Terms—Inertial navigation system (INS), magnetic field feature matching (MFM), pedestrian dead reckoning (PDR), pedestrian positioning, urban canyons.

I. INTRODUCTION

OCATION-BASED services (LBSs), such as pedestrian navigation, smart city, and express delivery, have emerged as a fundamental component of daily life [1]. The reliability and precision of positioning are critical to these services [2], [3]. Contemporary solutions for LBS predominantly use smartphones as the primary platform, necessitating high-precision positioning capabilities through these devices [4]. While the global navigation satellite systems (GNSSs)

Received 9 May 2025; revised 6 July 2025; accepted 26 September 2025. Date of publication 8 October 2025; date of current version 27 October 2025. This work was supported by the National Key Research and Development Program of China under Grant 2023YFC3604704 and Grant 2024YFB3909200. The Associate Editor coordinating the review process was Dr. Gabriele Patrizi. (Corresponding author: Jian Kuang.)

Shiyi Chen and Tingwei Wang are with the GNSS Research Center and the School of Geodesy and Geomatics, Wuhan University, Wuhan 430072, China (e-mail: chenshiyi@whu.edu.cn; 20173021200126@whu.edu.cn).

Jian Kuang, Yan Wang, and Xiaoji Niu are with the GNSS Research Center and the Hubei Technology Innovation Center for Spatiotemporal Information and Positioning Navigation, Wuhan University, Wuhan 430072, China (e-mail: kuang@whu.edu.cn; wystephen@whu.edu.cn; xjniu@whu.edu.cn).

Digital Object Identifier 10.1109/TIM.2025.3619223

provide accurate positioning in open outdoor environments, their performance significantly deteriorates in urban canyons due to signal attenuation and multipath effect [5], [6].

GNSS remains the primary research focus for pedestrian positioning due to its global coverage and infrastructureindependent characteristics in urban canyon environments. To address resulting positioning errors, research primarily focuses on error modeling [7], [8] and signal path identification [9], [10], [11], [12]. While these methodologies demonstrate potential for improving GNSS positioning accuracy, their correction efficacy remains limited when implemented in consumer-grade positioning terminals such as smartphones, primarily due to inherent signal acquisition limitations associated with low-cost antennas. Shadow matching (SM) represents another prominent GNSS-based positioning methodology. This approach fundamentally uses the GNSS signal obstruction effects generated by buildings and other urban structures to facilitate positioning [13], [14], [15]. However, commercial-grade GNSS chips embedded in smartphones exhibit significant signal-to-noise ratio (SNR) fluctuations, with signal intensity from a single satellite varying dramatically within short temporal intervals. These technological constraints currently limit SM's applicability for smartphone-based pedestrian positioning [16].

In addition to GNSS-based positioning methods, various other positioning solutions, such as WiFi, cellular networks, Bluetooth, magnetic field feature matching (MFM), and pedestrian dead reckoning (PDR), are extensively employed for pedestrian positioning in urban canyons. Zhao [17] and Italiano et al. [18] evaluated the positioning performance of cellular network signals in urban environments through simulation experiments and found that cellular network positioning methods encounter inaccuracies due to signal obstruction and multipath effects in urban canyons. Wang et al. [19] implemented a triangulation positioning method based on Bluetooth received signal strength (RSS), making it unreliable in urban canyons. Currently, the majority of wireless signalbased positioning methods employ fingerprint matching [20], [21], which achieves high positioning accuracy. Nevertheless, their performance is contingent upon the deployment of base stations and the accuracy of the fingerprint database, thus limiting their practicality in urban environments.

PDR is a relative positioning method wherein position errors accumulate proportionally to the distance traveled, leading to a significant degradation in positioning accuracy during extended navigation periods [22]. Currently, predominant PDR methodologies can be categorized into two primary paradigms: traditional step model-based PDR and deep learning-based PDR. The former relies on precise step detection, step length estimation, and heading estimation. However, the accuracy of these components is sensitive to variations in the pedestrian's handheld device posture [23], [24]. The latter is garnering considerable attention due to its enhanced robustness and noise resilience. Relevant research includes employing deep-learning methods to optimize key modules within the traditional PDR system, as well as constructing end-to-end neural network models for predicting pedestrian displacement (referred to as deep learning inertial odometry of Neural-PDR) [25], [26]. Nonetheless, existing PDR methods, irrespective of whether they are based on step model or deep learning, typically encounter issues of error accumulation and trajectory divergence, particularly in long-duration navigation scenarios. Consequently, PDR currently functions primarily as an auxiliary positioning technique, contributing to multisource fusion positioning schemes. The primary fusion methodologies currently encompass PDR/GNSS [27], [28], [29], [30], [31], PDR/wireless signals, and PDR/GNSS/wireless signals [32], [33]. While these positioning schemes can leverage PDR to achieve robust positioning results, the absolute positioning accuracy remains contingent upon the stability of GNSS signals and the precision of wireless signal fingerprint databases.

The geomagnetic field frequently exhibits distortions due to interference from the ferromagnetic materials in the surrounding environment, displaying distortion characteristics that correlate significantly with location, making them applicable for matching positioning. Compared to prevalent wireless signals, the magnetic field characteristics in urban environments offer advantages such as ubiquitous presence (i.e., no deployment), stability, and no attenuation by the human body. Currently, MFM for indoor positioning has been extensively researched [34], [35], [36], [37], achieving promising results. However, in urban canyon environments, the distribution of magnetic field characteristics has not been thoroughly studied. Even though the geomagnetic field may be distorted by ferromagnetic materials in these scenarios, its potential for positioning remains uncertain.

Therefore, this article aims to improve pedestrian positioning performance in complex urban canyon environments by leveraging the MFF. By analyzing the characteristics of MFF in urban canyons, the feasibility of employing MFM for positioning in such environments is demonstrated. Considering the diverse modes pedestrians hold smartphones, we use deep learning-based inertial odometry (Neural-PDR) as a substitute for traditional step model-based PDR, integrating it with MFM for positioning. Furthermore, given that smartphones typically do not support computationally intensive neural network models, the relative displacement increments generated by the lightweight learned inertial odometry neural network (LLIO-Net) [26] are employed to construct more accurate magnetic field strength sequences (MFSs), thereby significantly enhancing the precision and reliability of MFM. As the extended Kalman filter (EKF) lacks the capability to effectively integrate historical state information, the multistate constraint Kalman filter (MSCKF) is adopted to fuse the relative displacement increments and the MFM results, ultimately formulating a robust and highly reliable pedestrian positioning method for urban canyon environments. The main contributions of this article are as follows.

- 1) We analyzed the distribution of MFF in urban canyon environments by constructing magnetic field maps in three representative settings. The objective is to assess the feasibility of using MFF to assist pedestrian positioning in urban canyon environments characterized by poor GNSS signal quality and limited radio signal sources.
- 2) We proposed a pedestrian positioning method that integrates an inertial navigation system (INS), deep learning-based inertial odometry, and MFM. The algorithm uses displacement increments derived from the deep learning inertial odometry to generate MFS, thereby achieving a more stable MFM. Furthermore, the MSCKF is employed to fuse INS, the deep learning-derived relative displacement increments, and the MFM results. The algorithm demonstrates robust adaptability to various smartphone holding modes and performs effectively in environments including stairs, providing continuous and reliable positioning results for pedestrians in urban canyons.

The remainder of this article is organized as follows. Section II evaluates the distribution of MFF in urban canyons. Section III presents an overview of the proposed methods. Sections IV and V detail the MFM algorithm and the multisensor fusion algorithm proposed in this article, respectively. Section VI discusses the experimental setting and analyzes the results. Finally, we conclude this article and provide future work in Section VII.

II. ANALYSIS OF MAGNETIC FIELD CHARACTERISTICS IN URBAN CANYON

The geomagnetic field in indoor environments exhibits universally distorted characteristics due to the interference caused by ferromagnetic materials present in the building structures. These distortion characteristics are frequently associated with locations and can be leveraged for pedestrian positioning. In contrast, urban canyons experience relatively less interference from ferromagnetic materials. Intuitively, magnetic field characteristics in these scenarios are weaker than those in indoor environments. However, the complexity of the urban canyon environment may still lead to geomagnetic distortions that possess the capability to differentiate locations. Thus, in this section, we will focus on evaluating the magnetic field characteristics within urban canyon environments and analyzing their distribution, aiming to explore the feasibility of enhancing pedestrian positioning experiences in urban canyon environments.

In this article, we establish magnetic field fingerprint databases within three typical urban canyon environments, evaluating the distinguishability of location information derived from the MFFs in these databases to determine the applicability of MFF in urban canyon environments. The database construction employs the magnetic field fingerprinting scheme based on P-POS [38]. The equipment used for

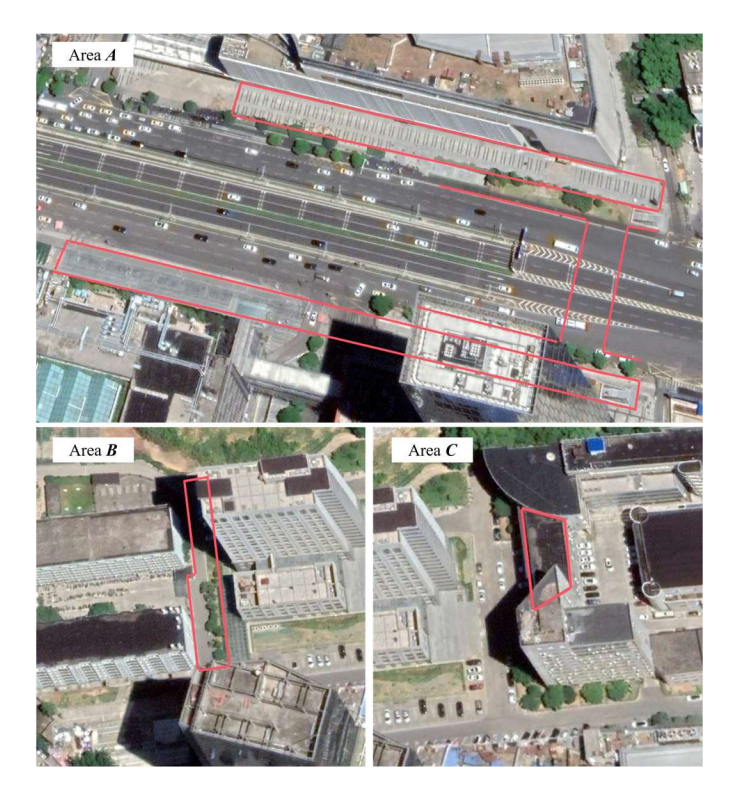


Fig. 1. Bird's eye views of the three test areas.

building the database includes the Huawei Mate 40 Pro and a foot-mounted inertial module. The test areas are located in JieDaoKou business district and Wuhan University. Area A encompasses the sidewalks in front of YinTai shopping center, the sidewalks in front of QunGuang shopping mall, and the underground pedestrian passage connecting the two sidewalks. This area is bordered by these two commercial buildings. Area B in Wuhan University consists of the western section of the sidewalk adjacent to the Xinghu Laboratory Building, which is flanked by the Xinghu Building on one side and a dormitory building on the other side. Area C in Wuhan University is under the overhead corridor that bridging two tower buildings, with several supporting columns standing in the area. Fig. 1 shows a bird's eye view of this area on Google Earth, where the region enclosed in a red box represents the areas where the magnetic field databases were constructed. The environmental characteristics of these three areas are detailed in Table I.

To construct the database for each area, a collector walked in a comprehensive S-shape pattern across the entire survey region, ensuring dense and uniform coverage. This systematic traversal was conducted at a normal walking pace. The data collection was performed during a weekday under clear and dry weather conditions and in periods of moderate pedestrian traffic, as the disturbances from other people are minor. Notably, instead of multiple repeated collections of the same path, our single-pass, area-wide S-shaped survey method is highly efficient; for instance, the complete database was constructed in approximately two hours. Further details regarding

TABLE I

DETAILED DESCRIPTION OF THE ENVIRONMENTAL

CHARACTERISTICS OF THE THREE AREAS

Area	Environmental Characteristics								
	The area is enclosed by high-rise building on both								
A	sides of the road and contains fixed structures.								
A	There are underground pedestrian passages and								
	subway tunnels beneath the ground.								
	There is a tall building that shields the interior from								
В	the sky, while on the other side of the path, there								
	are two multi-floor dormitory buildings.								
	The area is under an overhead corridor between								
\mathbf{C}	two tower buildings, with several supporting								
	columns containing ferromagnetic materials								

the magnetic field database construction can be found in our previous work [38].

Fig. 2 presents the magnetic field fingerprint databases for the three areas, with the vertical and horizontal axes representing the northward and eastward positions, respectively, while the color indicates the values of the magnetic field strength. Fig. 2(a)–(c) depicts the north, east, and vertical components of the magnetic field strength for the area, respectively.

Area A is interconnected through an underground pedestrian passage, linking the sidewalks on both sides of the street. And this scenario serves as a significant transportation hub, with metro tunnels also situated underground. Furthermore, the sidewalks contain numerous structures, such as benches and streetlights. Most of these structures contain ferromagnetic materials, which cause significant interference and result in distorted magnetic field characteristics. Analyzing the magnetic field fingerprint database, it can be observed that the magnetic fluctuations within a $2 \sim 3$ -m range typically exceed 50 mGauss. In some places, they even reach 400 mGauss. Area B, particularly on the side adjacent to the dormitory buildings, is in close proximity to the building's walls, where the reinforced concrete significantly influences the surrounding magnetic field. The closer one is to the building walls, the more pronounced the MFF become. The magnetic fluctuations within approximately 5 m of the building generally exceed 50 mGauss. In area C, the presence of columns containing ferromagnetic materials significantly affects the magnetic field distribution in this area. The MFF becomes increasingly pronounced as one approaches these columns, with fluctuations typically exceeding 30 mGauss within this environment.

Meanwhile, to provide a more intuitive visualization of the magnetic field distribution within urban canyon environments and to analyze the extent of its fluctuations, an additional trajectory was incorporated into Area A. Fig. 3 illustrates the trajectory on Google Earth alongside the corresponding magnetic field measurements in the *n*-frame. As depicted in the figure, the magnetic field characteristics along this trajectory exhibit significant spatial fluctuations. Notably, the amplitude of magnetic field strength fluctuations typically exceeds 50 mGauss over segments of the trajectory. Currently,

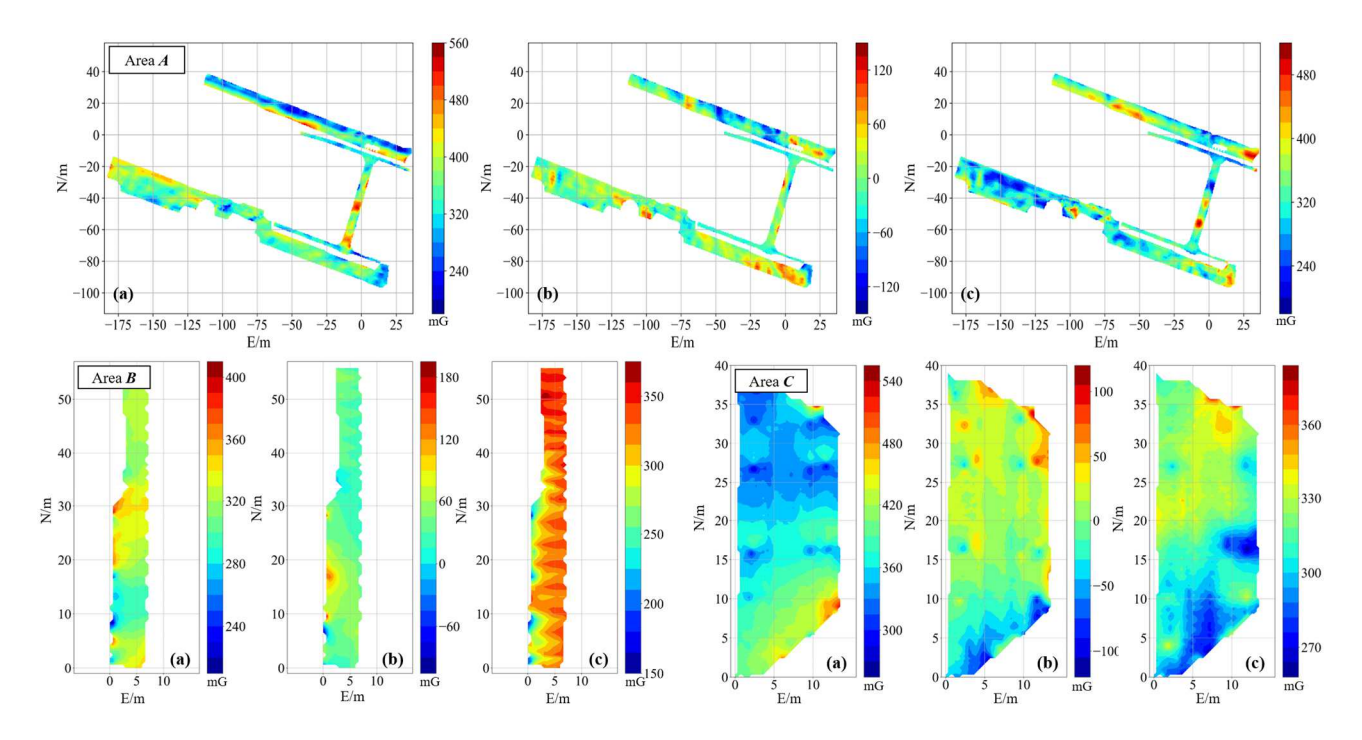


Fig. 2. Magnetic field fingerprint database of Area A, B and C. (a) North component. (b) East component. (c) Vertical component.

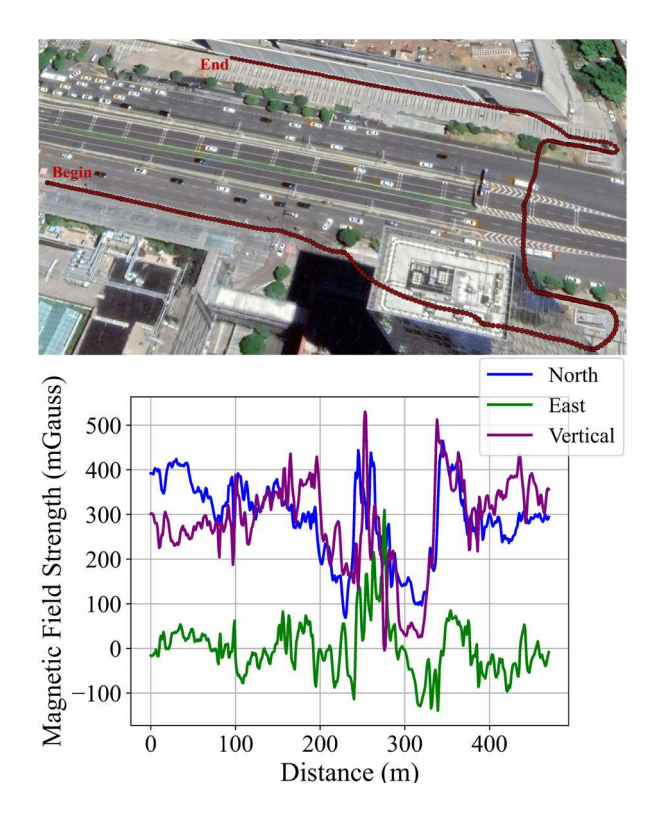


Fig. 3. Test trajectory in Area A (Google Earth View) and corresponding *n*-frame magnetic field.

the noise level of smartphone magnetometers is approximately 10 mGauss, indicating that the magnetic fluctuations in these scenarios can be detected. The magnetic field fluctuations in these environments can be easily detected, making it suitable for MFM.

Overall, in regions where magnetic field fluctuations significantly exceed the noise fluctuations of the smartphone's magnetometer, MFM can certainly be used for positioning; for example, in the three areas tested in this article (urban canyon environments), where environmental magnetic field distortions are formed due to interference from ferromagnetic buildings. Conversely, in areas without the ferromagnetic buildings, such as boulevards and playgrounds, the magnetic field does not exhibit positional distinctiveness and thus cannot be used for MFM.

Furthermore, it is noteworthy that the presence of abundant temporary ferromagnetic building materials within urban environments can potentially lead to localized temporal inconsistencies in the magnetic field database. However, considering the property that magnetic interference intensity from ferromagnetic materials attenuates with the inverse cube of distance, the field strength from such sources diminishes at distances beyond 1-2 m. Given that pedestrians typically maintain a safe clearance from such obstacles during navigation, they generally remain outside the effective range of this magnetic interference during actual walking. Moreover, temporary structures in urban environments are frequently sparsely distributed, which inherently mitigates the risk of widespread field superposition. Consequently, within urban canyon environments, the cumulative influence of temporary building materials on the overall magnetic field database is negligible. This suggests that the magnetic field database of urban environments exhibits robust long-term stability, rendering them suitable for MFM over considerable time spans. To empirically validate this assertion, the positioning experiments presented herein were performed incrementally over a period of 1-3 months following the initial construction of the magnetic field database. This temporal separation pro-

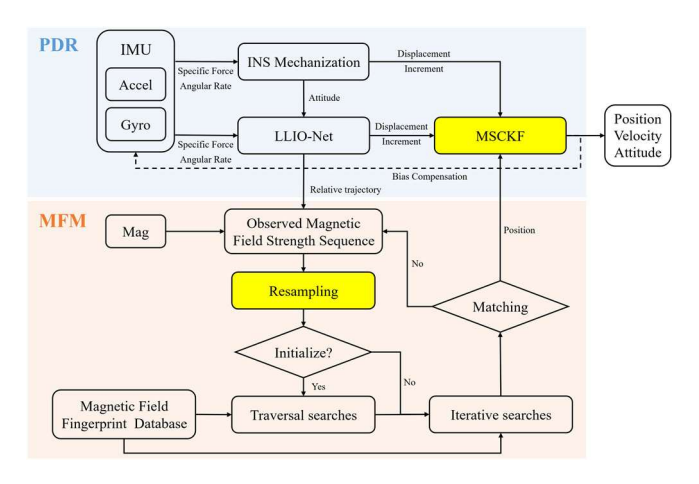


Fig. 4. Block diagram of the proposed positioning algorithm.

vides empirical evidence supporting the purported long-term stability of the magnetic field.

III. SYSTEM OVERVIEW

Given that the magnetic field at a specific location can encompass up to three dimensions of information, along with the observation that various locations exhibit similar magnetic field strengths, MFM typically necessitates sequence matching to enhance the distinctiveness of magnetic field fingerprints. The positioning accuracy of this method primarily depends on the completeness and continuity of the relative trajectory. However, under the complex dynamic conditions of pedestrians holding smartphones, the orientation of the smartphone sensors and the pedestrian's forward motion constantly vary. Moreover, in complex urban canyon environments, there are underground passages and overpasses that include stairs. In these scenarios, traditional PDR based on the step length model is inadequate to provide a reliable sequence and adversely affects the positioning performance of MFM. Therefore, in this article, we leverage the displacement increment output by the LLIO-Net to aid in developing a more accurate MFM solution. Furthermore, based on the results generated by MFM, we establish a more robust and reliable pedestrian positioning method.

The block diagram in Fig. 4 illustrates the architecture of system algorithm. The system comprises two primary modules: the PDR module and the MFM module. These two modules incorporate the traditional position loose integration algorithm. The PDR module consists of the LLIO-Net output and INS Mechanization. By integrating the displacement increments from the LLIO-Net as observation in Mechanization, a robust PDR is achieved (Neural-PDR). Given that the displacement increments from the LLIO-Net incorporate historical state information, the EKF is insufficient. Consequently, the state dimensions need to be expanded to form the MSCKF.

The MFM module relies on the relative displacement increments provided by LLIO-Net, in conjunction with magnetometer output, to generate MFS. Given that the magnetometer typically operates at a high frequency (e.g., 100 Hz), the generated MFS is also a high-frequency sequence and necessitates downsampling. Subsequently, the initialization of MFM is

performed, which initially involves a global search matching. Individual magnetic field strength or MFS generally lacks unique identifiability over extensive areas. Consequently, relying purely on MFFs is insufficient for achieving accurate initial position matching. Thus, during the system initialization stage, MFM necessitates complementary wide-area absolute positioning technologies to furnish an initial position estimate. Such positioning methodologies, including GNSS, wireless signals, and UWB, despite variations in their positioning accuracy, are all capable of providing the requisite initial position data for magnetic matching. Given that an in-depth analysis of these auxiliary positioning technologies is beyond the scope of this article, a simplified method was adopted: an approximate initial position is manually designated. This designated position subsequently served as the foundation for generating the initial MFS required to commence the initialization search and matching procedure.

Upon successful matching, the current position and heading angle are reset, followed by subsequent tracking matching. During the tracking matching phase, the search range is confined to the vicinity of the initialized position. Once matching is successful, the position obtained from MFM is incorporated into the filter as observation information.

IV. LLIO-NET ASSISTED MAGNETIC FIELD MATCHING ALGORITHM

Because of the frequent inadequacies of traditional PDR algorithms based on the step-length model in generating reliable sequences when pedestrians modify their smartphone-holding modes, the production of stable MFS sequences is hindered, subsequently impacting the positioning results of MFM. Consequently, in this section, we introduce an MFM algorithm assisted by LLIO-Net, which employs the stable and reliable relative trajectories generated by LLIO-Net to create MFS, thereby enhancing MFM performance. The subsequent discussion elucidates two pivotal components: the LLIO-Net model and the magnetic field matching.

A. LLIO-Net Model

LLIO-Net maps inertial measurement unit (IMU) data to pedestrian relative displacement over specified time intervals, enabling the estimation of displacement and associated uncertainty. This relative displacement, integrated with magnetometer outputs, facilitates the generation of MFS for MFM. LLIO-Net employs a residual multilayer perceptron (ResMLP) [39] architecture as its feature extractor, which uses fewer parameters compared to conventional multilayer perceptron (MLP) algorithms. The model comprises three primary components: a feature conversion section that transforms IMU data into a feature matrix, a feature extractor that derives salient information from the feature matrix, and a regression layer that estimates pedestrian displacement and corresponding uncertainty. The LLIO-Net model architecture is illustrated in Fig. 5.

The training of the LLIO-Net model necessitates parameter optimization to minimize prediction errors, and preprocessing of raw IMU data constitutes a prerequisite for model training.

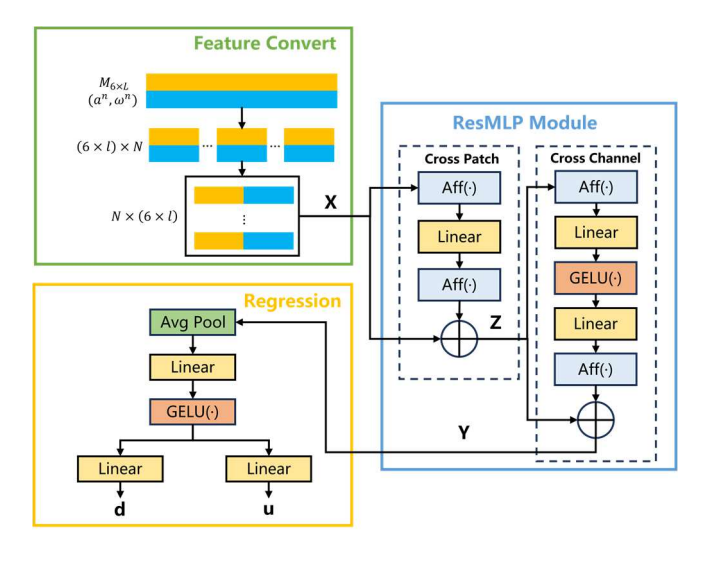


Fig. 5. LLIO-Net model architecture [26].

Initially, IMU measurements undergo zero-bias compensation, followed by transformation from the body frame (b-frame, denoted by the superscript b) to the navigation frame (n-frame, denoted by the superscript n) using attitude information. This transformation mitigates attitude and zero-bias effects, thereby providing stable input for subsequent model training.

The model training implements a dual-phase strategy employing mean square error (mse) and negative log-likelihood (NLL) loss functions. Initially, mse serves as the optimization criterion, quantifying the average squared differences between predictions and truth values, effectively capturing overall error trends. Training continues until mse convergence, indicating the model's acquisition of fundamental data characteristics. Subsequently, the optimization criterion transitions to NLL for refinement. NLL, commonly used in probabilistic frameworks, measures the discrepancy between predicted and actual probability distributions. By minimizing NLL, the model precisely calibrates its parameters to better approximate the data's probabilistic characteristics, thereby enhancing predictive accuracy. The training process concludes upon NLL convergence.

This article employs a comprehensive dataset comprising 40 h of pedestrian positioning data for model training. The dataset was curated to be highly diverse, covering a wide range of environments (e.g., underground garages, urban canyons, large buildings), pedestrian gaits, and natural smartphone holding modes (e.g., hand-held, in-pocket, swinging), with data collected from six participants using multiple smartphones to incorporate various sensor error characteristics, thereby enhancing model robustness. To rigorously assess the model's generalization capabilities and practical applicability, the dataset was randomly partitioned into three subsets: 80% for training, 10% for validation, and 10% for testing. The validation subset facilitates performance monitoring during training, mitigates overfitting, and optimizes hyperparameters. For the error analysis on the test subset, a high-precision reference trajectory was generated by Foot-INS. This system leverages a combination of zero-velocity updates (ZUPT) to suppress sensor drift, sparse control points for global correction, and a Rauch-Tung-Striebel (RTS) smoothing for optimal trajectory estimation. This method generates reference trajectories with decimeter-level accuracy, which serve as a reliable ground truth for the evolution of the LLIO-Net model. On the test subset, the trained LLIO-Net model demonstrates an average relative position error of 0.884 m for 1-min walked trajectories and an average relative error of 0.237 m for 10 m displacements.

B. Magnetic Field Matching

The MFS is generated by integrating the relative displacement output from LLIO-Net with magnetometer outputs. However, given that the magnetic field is a low-frequency, slowly varying signal, and the magnetometer's operating frequency is typically high (e.g., 100 Hz), in practical applications, the magnetometer's elevated sampling rate does not enhance positioning accuracy but increases computational burden. Consequently, resampling of the MFS is imperative.

As the MFS is generated through the relative displacement output by LLIO-Net, which lacks explicit step point information compared to PDR, fixed-frequency step points are employed for resampling, established at 2 Hz in this article. Initially, pedestrian dynamics are assessed, and step points are constructed exclusively under nonstatic conditions. Subsequently, during nonstatic periods, step points are extracted at a 2 Hz frequency, with their positions derived from LLIO-Net, which can be expressed as

$$\begin{bmatrix} N_k \\ E_k \end{bmatrix} = \begin{bmatrix} N_{k-1} + \Delta N_{\rm DL} \\ E_{k-1} + \Delta E_{\rm DL} \end{bmatrix}$$
 (1)

where N_k and E_k represent the north and east positions in the n-frame at the kth time step, respectively; $\Delta N_{\rm DL}$ and $\Delta E_{\rm DL}$ represent the components of position increment output by the network model in the north and east directions, respectively. The relative displacement increments generated by LLIO-Net exhibit smoothness, facilitating the search of matching sequences in magnetic field matching. The nearest attitude and magnetic field strength observations are used to complete the resampling process.

The resampled low-frequency MFS can be expressed as [37]

$$obs M = \begin{cases} \mathbf{r}_{1}^{n} \left(\mathbf{C}_{b}^{n} \right)_{1} \tilde{\mathbf{M}}_{1}^{b} \\ \cdots & \cdots \\ \mathbf{r}_{i}^{n} \left(\mathbf{C}_{b}^{n} \right)_{i} \tilde{\mathbf{M}}_{i}^{b} \end{cases}$$
 (2)

where *i* denotes the *i*th epoch in the MFS; $\mathbf{r}^n = [r_n \ r_e]$ represents the planar position vector, comprising its north and east components; \mathbf{C}_b^n is the direction cosine matrix from the *b*-frame to the *n*-frame, which is output by the INS; $\tilde{\mathbf{M}}^b$ represents the 3-D raw output of the magnetometer in the *b*-frame.

Given the assumption that a trajectory in the magnetic field fingerprint database exists that is identical to the pedestrian's actual trajectory, the MFM problem can be reframed as a task of matching relative and absolute trajectories [37]. The differences between these two trajectories primarily stem from rotation and translation. Consequently, the strategy adopted in

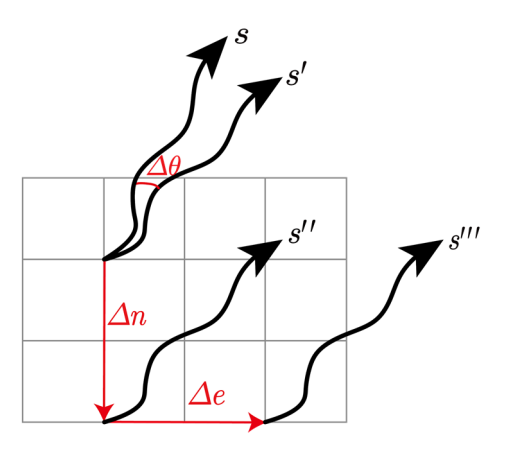


Fig. 6. Create potential candidate trajectories [35].

this article involves establishing maximum values and step sizes for translation and rotation on the relative trajectory generated by LLIO-Net, thereby creating a set of potential candidate trajectories, as illustrated in Fig. 6. By iterating through all candidate trajectories' corresponding magnetic field sequences, the similarity between the observed MFS and candidate MFS is computed using dynamic time warping (DTW). The candidate MFS exhibiting the highest DTW similarity is selected, and its corresponding candidate trajectory is considered to be the most accurate representation of the pedestrian's actual path. The positioning corresponding to the last point on this optimal trajectory is subsequently determined to be the pedestrian's current location.

While the MFS generated by LLIO-Net furnishes reliable directional information, it exhibits scale discrepancies concerning distance. The DTW algorithm can achieve superior matching between two sequences of different lengths by locally stretching the time series. The methodology is bifurcated into two phases: initially, the distance matrix between the target sequence and reference sequences is computed. Subsequently, the path exhibiting the minimal cumulative sum of elements from the bottom-right to the top-left of the distance matrix is identified. The process of identifying the optimal path is delineated as follows: commencing from the terminal grid point (i, j) of the two sequences, the search progresses to the preceding grid points (i-1, j-1), (i-1, j), and (i, j-1), selecting the grid point with the smallest distance among the three as the preceding grid point. The cumulative distance of the optimal path can be expressed as

$$D_{i,j} = d_{i,j} + \min \left(D_{i-1,j-1}, D_{i-1,j}, D_{i,j-1} \right)$$
 (3)

where $d_{i,j}$ represents the local distance; $D_{i,j}$ denotes the minimum cumulative distance from the starting point to the grid point (i, j). Following each successful magnetic field matching, to ensure the precision of subsequent positioning, it is necessary to reset the MFS, encompassing both position and heading resets. The objective of the position reset is to align the MFS position with the corresponding location in the successfully matched magnetic fingerprint database. The position reset can be mathematically expressed as

$$\begin{bmatrix} dn \\ de \end{bmatrix} = \mathbf{r}_{\text{raw}}^n - \mathbf{r}_{\text{cMFM}}^n$$

$$\mathbf{r}_{\text{new}}^{n} = \mathbf{r}_{\text{dMFM}}^{n} + \mathbf{r}_{\text{cMFM}}^{n} + \begin{bmatrix} \cos \psi - \sin \psi \\ \sin \psi & \cos \psi \end{bmatrix} \begin{bmatrix} dn \\ de \end{bmatrix}$$
 (4)

where r_{raw}^n and r_{new}^n denote the positions of the original and updated MFS, respectively; r_{cMFM}^n represents the central coordinate of the magnetic grid following successful matching; r_{dMFM}^n indicates the grid position offset; ψ is the heading offset. The objective of heading reset is to align the initial heading of the MFS with the heading of the most similar trajectory in the magnetic fingerprint database. The mathematical formulation for heading reset can be expressed as

$$\boldsymbol{C}_{b,\text{new}}^{n} = \begin{bmatrix} \cos \psi - \sin \psi & 0\\ \sin \psi & \cos \psi & 0\\ 0 & 0 & 1 \end{bmatrix} \boldsymbol{C}_{b,\text{raw}}^{n}$$
 (5)

where $C_{b,\text{new}}^n$ and $C_{b,\text{raw}}^n$ represent the attitude matrices of the original and updated MFS, respectively. Through the reset of position and heading, the MFS achieves alignment with the most congruent trajectory in the magnetic fingerprint database, thereby mitigating cumulative errors and enhancing the precision of positioning.

V. INS/LLIO-NET/MFM MULTISOURCE FUSION

Any single sensor is difficult to provide reliable and continuous localization. Consequently, it is imperative to use multisensor fusion to enhance positioning performance. In this article, we integrate INS, LLIO-Net, and MFM through the MSCKF, thereby establishing a more robust positioning scheme.

A. Filter Design

The MSCKF effectively leverages historical state information, thereby overcoming the limitations inherent in the EKF, which relies exclusively ON current state estimates. Given that the displacement increments generated by LLIO-Net incorporate historical information, this article adopts MSCKF to integrate multiple positioning sources. With INS as the core, we use the position increments output by LLIO-Net and magnetic field matching positioning results to correct the system's positioning errors. The traditional INS algorithm considers numerous minor error corrections, which are less effective for consumer-grade IMUs embedded in smartphones due to their high noise levels. Consequently, the INS algorithm implemented in this article only considers sensor noise and bias effects, while disregarding minor correction terms such as Earth rotation. The detailed derivation of the kinematic equations for such a simplified model, the linearization process for the error state, and the formulation of the continuous-time dynamics matrix and noise-driving matrix are well-established and thoroughly described in [37] and other seminal works on visual-inertial fusion [40]. Our work directly adopts these established models for state propagation.

Because of the incorporation of position state information from both current and previous epochs, the system state vector comprises two principal components: the INS error state vector and the position error state vector from previous epochs, which can be mathematically expressed as

$$\delta \mathbf{x} = \begin{bmatrix} \delta \mathbf{x}_{\text{ins}} & \delta \mathbf{r}_{\text{pre}} \end{bmatrix} \tag{6}$$

where $\delta r_{\rm pre}$ denotes the position error state vector from previous epochs, and $\delta x_{\rm ins}$ represents the INS error state vector at the current epoch, comprising the position error δr^n , velocity error δv^n , attitude error ϕ , gyroscope bias error δb_g , accelerometer bias error δb_a . In addition, we introduce a scale factor error δS . It is crucial to clarify that δS here does not refer to the conventional scale factor errors of the IMU sensors (i.e., accelerometer or gyroscope). Instead, it represents the scale factor error of the relative displacement increment provided by LLIO-Net. A 1-D model is adopted for the scale factor error to mitigate the estimation instability across three degrees of freedom and to account for its manifestation as a slowly varying bias under dynamic conditions [26]. The INS error state vector $\delta x_{\rm ins}$ can be expressed as

$$\delta \mathbf{x}_{\text{ins}} = \left[\left(\delta \mathbf{r}^n \right)^T \left(\delta \mathbf{v}^n \right)^T \boldsymbol{\phi}^T \delta \boldsymbol{b}_g^T \delta \boldsymbol{b}_a^T \delta S \right]. \tag{7}$$

The state transition equation characterizes the temporal evolution of the state vector. During the state transition phase, the computation of historical position states is not necessitated. The state transition equation can be formulated as

$$\delta \mathbf{x}_{k,k-1} = \mathbf{\Phi}_{k,k-1} \delta \mathbf{x}_{k-1} \tag{8}$$

where $\Phi_{k,k-1}$ is the state transition matrix from the (k-1)th epoch to the kth epoch, which is expressed as

$$\Phi_{k,k-1} = \begin{bmatrix}
\Phi_{16} & \mathbf{0}_{3\times 16} \\
\mathbf{0}_{16\times 3} & \mathbf{I}_{3}
\end{bmatrix}$$

$$\Phi_{16} = \begin{bmatrix}
\Phi_{15} & \mathbf{0}_{1\times 15} \\
\mathbf{0}_{15\times 1} & \exp\left(-\frac{\Delta t}{\tau_{S}}\right)
\end{bmatrix}$$
(9)

where Φ_{15} denotes the 15-D INS error state transition matrix, as elaborated in [41]; Δt represents the temporal between consecutive epochs, and τ_S indicates the correlation time of first-order Markov Process for scale factor error. The covariance matrix transition equation represents the evolution of system uncertainty characterization between consecutive epochs, which can be mathematically formulated as

$$\mathbf{P}_{k,k-1} = \mathbf{\Phi}_{k,k-1} \mathbf{P}_{k-1} \mathbf{\Phi}_{k,k-1}^T + \mathbf{\Gamma}_{k-1} \mathbf{Q}_{k-1} \mathbf{\Gamma}_{k-1}^T$$
 (10)

where **P** denotes the covariance matrix of the system state; **Q** represents the noise matrix characterizing system uncertainties.

When observations are accessible, the measurement equation can be established, which is mathematically expressed as

$$\mathbf{z}_k = \mathbf{H}_k \mathbf{x}_k + \mathbf{v}_k \tag{11}$$

where \mathbf{z}_k represents the observation vector comprising the difference between predictions and observations; \mathbf{H}_k denotes the measurement design matrix; \mathbf{v}_k characterizes the observation noise. The measurement update equations for the system error state and its associated covariance matrix can be formulated as

$$\mathbf{K}_{k} = \mathbf{P}_{k/k-1} \mathbf{H}_{k}^{T} \left(\mathbf{H}_{k} \mathbf{P}_{k/k-1} \mathbf{H}_{k}^{T} + \mathbf{R}_{k} \right)^{-1}$$

$$\hat{\mathbf{x}}_{k} = \hat{\mathbf{x}}_{k/k-1} + \mathbf{K}_{k} \left(\mathbf{z}_{k} - \mathbf{H}_{k} \hat{\mathbf{x}}_{k/k-1} \right)$$

$$\mathbf{P}_{k} = \left(\mathbf{I} - \mathbf{K}_{k} \mathbf{H}_{k} \right) \mathbf{P}_{k/k-1} \left(\mathbf{I} - \mathbf{K}_{k} \mathbf{H}_{k} \right)^{T} + \mathbf{K}_{k} \mathbf{R}_{k} \mathbf{K}_{k}^{T}$$
(12)

where **K** denotes the Kalman gain matrix, and **R** represents the observation noise covariance matrix characterizing measurement uncertainties. It is imperative to emphasize that the measurement update process of the filter is based on the correlation between historical keyframe and the current keyframe. Consequently, the preservation of historical keyframe states within the filter is essential and is achieved through state cloning. Given that the measurement equations are independent of velocity and attitude, only the positional states corresponding to the current position necessitate replication. The associated covariance matrix for keyframe can be formulated as

$$\mathbf{P}^{\text{new}} = \begin{bmatrix} \mathbf{I}_{6} & 0_{6\times3} & 0_{6\times3} \\ 0_{3\times6} & \mathbf{I}_{3} & 0_{3} \\ \mathbf{A} & 0_{3} & \mathbf{I}_{3} \end{bmatrix} \mathbf{P} \begin{bmatrix} \mathbf{I}_{6} & 0_{6\times3} & 0_{6\times3} \\ 0_{3\times6} & \mathbf{I}_{3} & 0_{3} \\ \mathbf{A} & 0_{3} & \mathbf{I}_{3} \end{bmatrix}^{T}$$

$$\mathbf{A} = \begin{bmatrix} \mathbf{I}_{3} & 0_{3} \end{bmatrix}. \tag{13}$$

B. Displacement Increments Update

The output of LLIO-Net is a relative displacement vector over a period. This vector is derived from the raw IMU output and projected from the b-frame to the n-frame using the attitude obtained from INS mechanization, prior to being input into the network model. Direct implementation of this displacement increment as an observation would introduce constraints on absolute heading information. Given that both the prediction phase and observation update phase are dependent on this attitude information, this would effectively result in the filter using its self-generated absolute heading information for self-correction. Consequently, when employing this displacement increment as observational data, it becomes imperative to mitigate the influence of absolute heading. This article accomplishes this objective by transforming the displacement increment from the *n*-frame to the local horizontal gravity coordinate frame (n'-frame, denoted by the superscript n'). The mathematical formulation for the observation update equation pertaining to the displacement increment can be expressed as

$$\delta z_{\text{dpos}}
= \widehat{z}_{\text{dpos}} - \widetilde{z}_{\text{dpos}}
= C_{\text{yaw}}^{T} \left(\mathbf{r}^{n} - \mathbf{r}_{\text{pre}}^{n} \right) - S \cdot d\mathbf{pos}_{n'}
= C_{\text{yaw}}^{T} \left(\mathbf{r}^{n} + \delta \mathbf{r}^{n} - \mathbf{r}_{\text{pre}}^{n} - \delta \mathbf{r}_{\text{pre}}^{n} \right) - (S + \delta S) \cdot d\mathbf{pos}_{n'}
= C_{\text{yaw}}^{T} \delta \mathbf{r}^{n} - C_{\text{ins}}^{T} \delta \mathbf{r}_{\text{pre}}^{n} - d\mathbf{pos}_{n'} \cdot \delta S$$
(14)

where \tilde{z}_{dpos} and \hat{z}_{dpos} represent the displacement increment measurement vector and its corresponding prediction, respectively; $dpos_{n'} = \left[dp_x \ dp_y \ dp_z\right]_{n'}^T$ denotes the 3-D relative displacement increment in the n'-frame generated by LLIONet; C_{yaw} represents the rotation matrix corresponding to the heading angle; S indicates the scaling factor. Considering that the relative displacement output by LLIO-Net demonstrates a certain magnitude of scale error, it is essential to estimate the scaling factor to mitigate its influence.

Meanwhile, LLIO-Net sporadically generates anomalous displacement predictions in practical applications. Consequently, this article employs the chi-squared test to evaluate and eliminate these statistical outliers, which can be mathematically expressed as

$$C_{\text{yaw}}^{T} \left(\mathbf{r}^{n} - \mathbf{r}_{\text{pre}}^{n} \right) - \text{dpos}_{n'}|_{\mathbf{H}_{\text{nosn}}^{T}} \mathbf{PH}_{\text{qoon}} + \mathbf{R}_{\text{doss}} < \alpha$$

$$\mathbf{H}_{\text{dpos}} = \begin{bmatrix} \mathbf{C}_{\text{yaw}}^T & 0_3 & 0_3 & 0_3 & 0_3 & -\text{dpos }_{n'} & -\mathbf{C}_{\text{ins}}^T \end{bmatrix}$$
 (15)

where \mathbf{H}_{dpos} denotes the design matrix of (14); \mathbf{R}_{dpos} represents the covariance matrix of the displacement increment generated by LLIO-Net; α is the critical value for the chi-squared test. The critical value established in this article is fixed at 11.345, corresponding to a confidence level of 99% for a chi-squared distribution with three degrees of freedom. Furthermore, to prevent filter divergence due to continuous rejection of all displacement observations, if the detection metric is rejected for three consecutive iterations, the current observation is mandatorily accepted.

C. MFM Positioning Update

In urban canyon environments, the magnetic field is significantly distorted, generating distinctive characteristics that facilitate high-precision pedestrian positioning through MFM. However, in practical applications, due to factors such as magnetic field similarity, extraneous signal interference, and database precision constraints, real-time measurements may inaccurately correlate with erroneous locations in the database, resulting in significant positional discrepancies. Consequently, exclusive dependence on MFM-derived positioning results lacks requisite robustness, necessitating supplementary calibration and integration methodologies.

Therefore, this article conceptualizes the positioning results obtained from MFM as observations rather than definitive positioning outcomes. Specifically, we integrate the MFM-derived positions as observations for correction. The position measurement equation can be mathematically expressed as

$$\delta z_r = \hat{r}_{\text{ins}}^n - \tilde{r}_{\text{MM}}^n = \delta r^n + n_{\text{MFM}}$$
 (16)

where $\hat{\mathbf{r}}_{\text{ins}}^n = \left[\hat{r}_n \ \hat{r}_e\right]$ represents the horizontal position estimated by INS; $\tilde{r}_{\text{MM}}^n = \left[\tilde{r}_n \ \tilde{r}_e\right]$ denotes the horizontal position derived from MFM; \mathbf{n}_{MFM} represents the measurement noise associated with the position observations. The measurement noise can be quantified using the gradient and residual error of the MFS as follows:

$$\mathbf{n}_{\text{MFM}} = \left(\mathbf{H}^{T}\mathbf{H}\right)^{T}\mathbf{n}_{0}$$

$$\mathbf{n}_{0} = \sqrt{\frac{\sum_{j=0}^{k-1} |\tilde{\mathbf{M}}_{j}^{n} - \mathbf{M}_{j}^{n}|}{k}}$$

$$\mathbf{H} = \left[\mathbf{H}_{0} \cdots \mathbf{H}_{k-1}\right]^{T}$$

$$\mathbf{H}_{j} = \left(\frac{\partial \mathbf{M}^{n}\left(\mathbf{r}_{j}\right)}{\partial n} \frac{\partial \mathbf{M}^{n}\left(\mathbf{r}_{j}\right)}{\partial e}\right) \frac{\partial \mathbf{r}_{j}\left(\xi\right)}{\partial \xi}$$
(17)

where $\widetilde{\mathbf{M}}^n$ denotes the magnetometer output transformed to the *n*-frame; \mathbf{M}^n represents the reference magnetic field vector retrieved from the magnetic field fingerprint database in the *n*-frame; $(\partial \mathbf{M}^n(r))/\partial n$ and $(\partial \mathbf{M}^n(r))/\partial e$ represent the magnetic field gradients in the northward and eastward directions, respectively; $(\partial r(\xi))/\partial \xi$ signifies the partial derivative of the absolute position with respect to translation and rotation. The definitions of the magnetic field gradients and the partial derivative of the absolute position are presented in [37].

VI. EXPERIMENTS AND RESULTS

A. Experiments Descriptions

To validate the positioning performance of the proposed pedestrian positioning method in urban canyon environments, multiple field tests were conducted in the constructed magnetic field fingerprint database. These tests were entirely conducted in Area A, considering its adequate spatial extent, which incorporated representative GNSS-denied areas typical of urban environment, including pedestrian walkways enclosed by highrise buildings and subterranean pedestrian passages. Although Areas B and C exemplify typical urban environments, their restricted spatial dimensions and relatively uniform environmental characteristics inadequately represent the diverse scenarios encountered in urban canyons. Area A incorporates the environmental characteristics present in Areas B and C, ensuring that experimental results obtained in Area A more accurately reflect the algorithm's positioning performance in urban canyon environments.

The total length of the testing routes extended approximately 8.25 km. The test equipment comprised smartphones and a foot-mounted module, with smartphones used for positioning test data collection, while the foot-mounted module generated positional reference values through P-POS [38], which achieves decimeter-level accuracy. Meanwhile, to evaluate the generalizability of the proposed algorithm, two distinct smartphones were employed for data collection (Huawei-Mate40Pro and HonorMagic6). The experiment encompassed 12 tests for assessing the positioning performance of the proposed method: tests 1–6 using the HuaweiMate40Pro, and tests 7–12 employing the HonorMagic6.

Furthermore, to closely simulate diverse smartphone-holding postures during pedestrian movement, participants conducted tests with multiple smartphone-holding modes, including stable handheld, swinging, and dynamic alternation between stable handheld and swinging. The stable handheld encompassed various modes such as flat-holding, calling, and horizontal or vertical photography. Specifically, tests 1, 2, 7, and 8 were executed under the stable flat-holding mode, while the remaining tests implemented randomized holding modes throughout the walking assessment. Each test was conducted independently, ensuring trajectory uniqueness between successive tests; that is, participants walking within the experimental area while implementing arbitrary smartphone-holding and movement trajectories.

B. Positioning Performance

This section presents a comparative analysis of four distinct positioning schemes to validate the feasibility and effectiveness of the proposed method. The evaluated positioning schemes include: 1) the Strapdown PDR algorithm developed by Kuang, referred to as S-PDR [42]; 2) the PDR algorithm based on LLIO-Net, referred to as Neural-PDR; 3) the MFM using relative trajectory generated through S-PDR, which implements MFM positioning results to mitigate S-PDR cumulative errors, referred to as S-PDR/MFM [37]; and 4) the positioning method proposed in this article, referred to as Neural-PDR/MFM. The test trajectories consist of straight

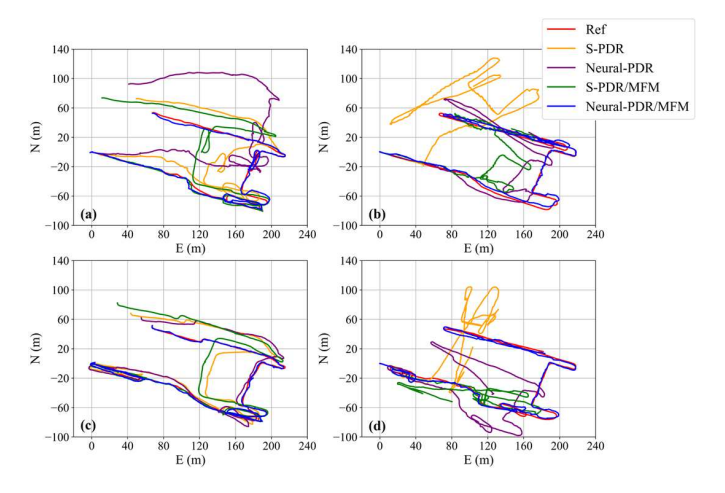


Fig. 7. Trajectories of the reference, S-PDR, Neural-PDR, S-PDR/MFM, Neural-PDR/MFM across four tests. (a) Test 1, (b) Test 3, (c) Test 7, and (d) Test 9.

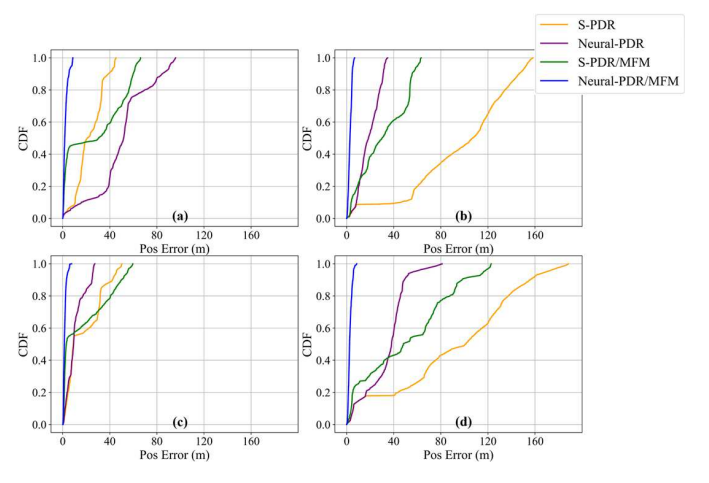


Fig. 8. CDF of S-PDR, Neural-PDR, S-PDR/MFM, Neural-PDR/MFM across four tests. (a) Test 1, (b) Test 3, (c) Test 7, and (d) Test 9.

lines and irregular curves, with pedestrians holding the smartphone in arbitrary modes during most test, demonstrating the methodology's adaptability to various pedestrians' trajectories without being influenced by the smartphone holding mode. Fig. 7 illustrates the comparative trajectories of the reference, S-PDR, Neural-PDR, S-PDR/MFM, and Neural-PDR/MFM of tests 1, 3, 7, and 9, where red, yellow, purple, green, and blue lines denote the reference, S-PDR, Neural-PDR, S-PDR/MFM, and Neural-PDR/MFM trajectories, respectively. Fig. 8 presents the cumulative distribution function (cdf) analysis for S-PDR, Neural-PDR, S-PDR/MFM, and Neural-PDR/MFM across these four tests. Tests 1 and 7 were conducted using Huawei and Honor smartphones under the stable flat-holding mode, while tests 3 and 9 were performed under variable smartphones-holding modes; the remaining 8 test trajectories are similar. Analysis of the trajectories reveals that those generated by S-PDR exhibit variable scales and deformation errors across different tests. Notably, S-PDR demonstrates inadequate performance in stair scenarios, resulting in substantial scale errors in such environments. In contrast, Neural-PDR exhibits relatively minor scale and

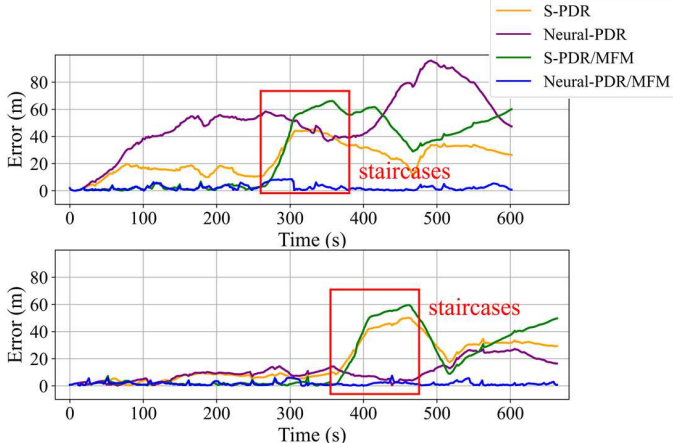


Fig. 9. Error Curves for S-PDR, Neural-PDR, S-PDR/MFM, and Neural-PDR/MFM in Test 1 and Test 7.

deformation errors compared to S-PDR, particularly demonstrating superior performance with smaller scale errors in stair environments.

Fig. 9 illustrates the error curves for tests 1 and 7, corresponding to two datasets under stable flat-holding mode, and indicates that in planar scenarios, Neural-PDR exhibits lower positioning accuracy compared to S-PDR when the smartphone maintains a stable flat-holding posture. Neural-PDR generally relies on extensive training data, and the variations in stable flat-holding positions among different pedestrians can be substantial. The training dataset may not encompass specific pedestrian patterns, potentially leading to reduced positioning performance across different pedestrians. Conversely, S-PDR identifies the pedestrian's smartphone flat-holding position through predetermined criteria, ensuring stable estimation of the mounting angle. This stability enables S-PDR to maintain more consistent performance across various pedestrians, resulting in superior positioning accuracy. Nevertheless, both Neural-PDR and S-PDR maintain a precise trajectory in planar scenarios under a stable flat smartphone-holding mode. Consequently, S-PDR and Neural-PDR enable accurate MFS generation under stable flat smartphone-holding mode in planar scenarios. For example, during the initial trajectory segments, where pedestrians traversed planar environments, the positioning accuracy of S-PDR/MFM demonstrates equivalence to Neural-PDR/MFM, both achieving high precision levels. However, upon transitioning to stair environments, the significant scale errors in S-PDR result in substantial inaccuracies in the generated MFS, thereby compromising the achievement of precise MFM results.

Meanwhile, during transitions in smartphone-holding modes, S-PDR may fail to accurately estimate the angular difference between smartphone orientation and pedestrian movement direction, resulting in sudden directional shifts and subsequent trajectory distortions. Fig. 10 illustrates the error curves for tests 3 and 9, which demonstrate that during alterations in pedestrian smartphone-holding modes, S-PDR exhibits significant shape deformations, generating errors that preclude the production of reliable shape MFS, thus preventing effective MFM. Conversely, Neural-PDR

TABLE II
RMS, 68 % and 95 % of the Position Errors of S-PDR, Neural-PDR, MFM/S-PDR, and MFM/Neural-PDR in 12 Tests

Test	S-PDR (m)			Neural-PDR (m)			MFM/S-PDR (m)			MFM/Neural-PDR (m)			Distance
1681	RMS	68%	95%	RMS	68%	95%	RMS	68%	95%	RMS	68%	95%	(m)
1	25.86	31.44	43.96	55.58	55.16	90.93	36.93	46.71	61.96	3.10	2.66	7.59	648.46
2	33.61	32.55	69.95	29.85	30.21	55.28	13.04	3.95	29.80	2.15	1.81	4.20	825.47
3	105.20	122.07	152.31	20.92	25.26	32.14	37.28	49.95	60.28	2.90	3.83	5.31	697.44
4	161.54	180.25	264.43	26.50	27.98	52.27	12.60	11.61	24.31	4.60	4.39	8.90	716.83
5	15.78	17.69	23.93	26.92	30.35	51.46	27.65	28.83	54.60	3.89	4.22	6.55	662.57
6	123.76	151.37	172.57	10.37	11.06	17.77	15.48	19.14	28.45	3.33	3.39	6.21	659.51
7	23.40	29.74	45.61	13.05	11.63	25.73	26.34	26.05	55.09	2.10	1.96	4.47	704.83
8	75.33	82.17	112.54	74.71	87.28	101.07	19.97	14.04	47.92	1.95	1.94	3.95	613.72
9	104.96	124.25	169.53	37.89	42.16	56.45	62.54	72.37	116.25	3.26	3.35	5.79	761.32
10	107.5	122.96	192.28	37.87	45.50	55.76	84.06	106.41	124.84	2.91	3.30	5.01	653.87
11	88.6	69.68	210.52	18.04	20.00	24.52	46.26	54.78	63.65	2.51	2.57	4.50	607.71
12	91.83	102.00	162.82	24.98	27.90	50.46	77.51	93.02	111.54	3.10	3.20	5.46	674.21
Mean	79.78	88.85	135.04	31.39	34.54	51.15	38.31	43.91	64.89	2.98	3.05	5.66	685.50

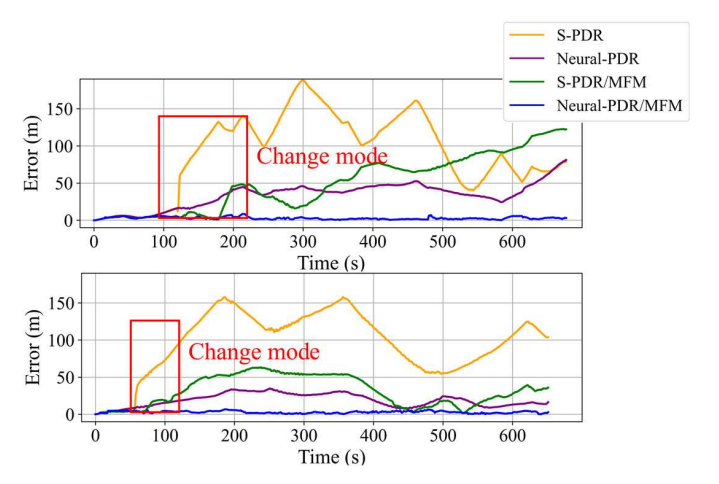


Fig. 10. Error curves for S-PDR, Neural-PDR, S-PDR/MFM, and Neural-PDR/MFM in Test 3 and Test 9.

demonstrates superior adaptability to varying smartphone-holding modes, maintaining trajectory shape accuracy despite changes in smartphone-holding modes. Furthermore, Neural-PDR exhibits enhanced performance in stair environments, producing minimal scale errors. Consequently, Neural-PDR consistently generates high-quality MFS, facilitating precise and reliable MFM positioning.

The statistical analysis of the root mean square (rms), 68% and 95% of the position errors from the 12 tests are summarized in Table II. The mean position errors of rms, 68% and 95% for S-PDR are 79.78, 88.85, and 135.04 m; for Neural-PDR, 31.39, 34.54, and 51.15 m; for S-PDR/MFM, 38.31, 43.91, and 64.89 m; and for Neural-PDR/MFM, 2.98, 3.05, and 5.66 m. Although the relative trajectories generated by Neural-PDR demonstrate heading and scale errors, they effectively facilitate the implementation of MFM. Meanwhile, the statistical results indicate negligible performance variations between these two smartphones, substantiating the universal applicability and device-independent characteristics of the proposed method.

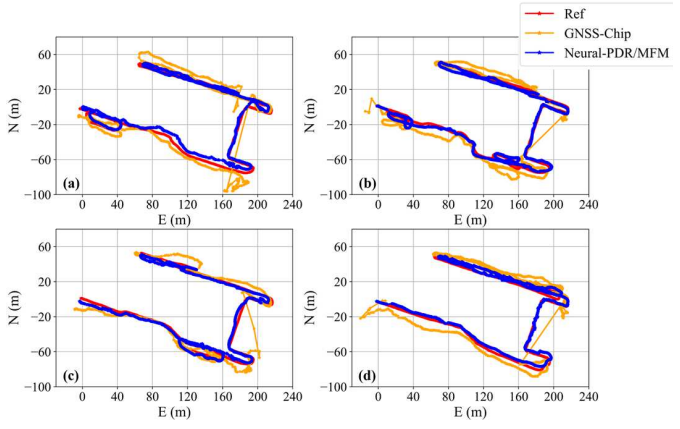


Fig. 11. Trajectories of the reference truth, GNSS chips, and proposed Neural-PDR/MFM for four independent tests. (a) Test II. (b) Test II. (c) Test III. (d) Test IV. Note: The trajectories in (a)–(d) are from four distinct experimental runs.

Overall, within the proposed positioning framework, Neural-PDR demonstrates superior MFS accuracy in stair environments, consequently achieving enhanced MFM precision. Additionally, during complex smartphone-holding modes transitions, S-PDR encounters mounting angle estimation difficulties, resulting in trajectory distortions. Neural-PDR, however, uses the displacement increment generated by LLIO-Net, circumventing mounting angle estimation challenges and achieving enhanced trajectory precision. Meanwhile, to quantitatively demonstrate the superiority of the proposed Neural-PDR/MFM algorithm, an accuracy improvement analysis was conducted. The improvement metrics were calculated by comparing the rms of positioning errors across different methods. The analytical results indicate that the proposed Neural-PDR/MFM method achieves a 90.51% improvement in positioning accuracy compared to Neural-PDR, and a 92.22% enhancement relative to S-PDR/MFM.

Furthermore, to validate the efficacy of the proposed method in smartphone positioning, a comprehensive comparative anal-

TABLE III
RELATIVE ERROR PERCENTAGE OF THE PROPOSED METHOD ACROSS VARIOUS SMARTPHONE-HOLDING MODES

Test	Hold-1 (%)	Swing-1 (%)	Hold-2 (%)	Swing-2 (%)		
1	0.515	0.929	0.592	1.055		
2	0.450	0.875	0.571	1.063		
3	0.446	0.94	0.669	0.929		
Mean	0.471	0.915	0.611	1.016		

ysis was conducted between positioning results obtained from built-in GNSS chips and the proposed method. Fig. 11 presents comparative trajectories from four experimental tests. The analysis demonstrates that in urban canyon environments, smartphone GNSS chip outputs exhibit significant positioning errors, typically ranging from 5 to 10 m, with maximum errors reaching approximately 20 m in specific locations. Notably, in complex environments with GNSS signal obstruction, such as underground pedestrian passages, smartphone GNSS chips cease to provide positioning outputs entirely, highlighting their environmental limitations. In contrast, the proposed method maintains consistent and reliable positioning capabilities throughout these evaluation zones, achieving markedly improved accuracy compared to GNSS chip outputs. Thus, the proposed method offers enhanced positioning performance for smartphone users, particularly in challenging environments where GNSS signals are compromised.

C. Performance Analysis and Influencing Factors

This section analyzes the factors affecting the positioning performance of the Neural-PDR/MFM method through the ablation experiments. We will explore the influences on the proposed method from the perspectives of Neural-PDR and MFM. From the Neural-PDR perspective, the primary factor impacting performance is the mode in which pedestrians hold their smartphones. The modes of smartphone holding can be categorized into the following types: stable handheld, swinging, transitions between stable handheld modes, and transitions between handheld and swinging. By testing the positioning errors of the proposed algorithm on flat ground under these four smartphone-holding modes, we aim to analyze the impact of different smartphone modes on positioning performance. The data collect scheme for these four modes is as follows: walking randomly while holding the phone flat, referred to as "Hold-1"; walking while holding the phone in a swinging mode, referred to as "Swing-1"; walking while holding the phone steadily, but switching between various modes, including flat holding, calling, and horizontal and vertical photography, referred to as "Hold-2"; walking while switching between handheld and swinging modes, referred to as "Swing-2." Three sets of data are collected for each mode, with each route approximately 300 m.

Because of the varying lengths of data collected across these four modes, it is necessary to use the relative error percentage to evaluate the accuracy for each mode. Table III presents the statistical values of the relative error percentage

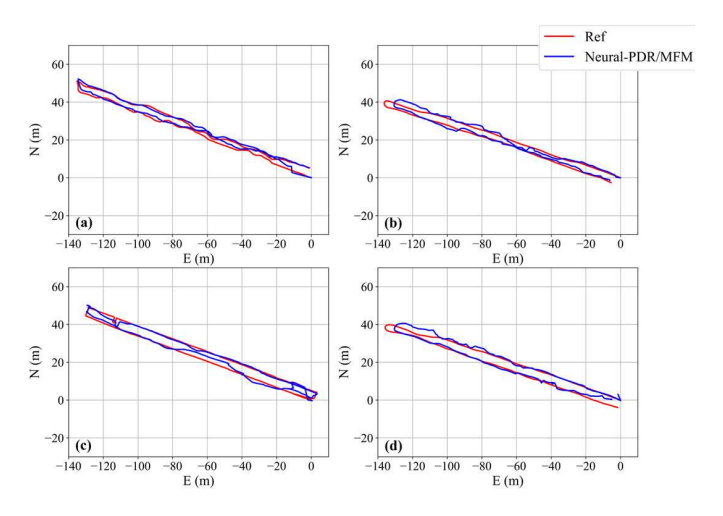


Fig. 12. Trajectories of the reference truth and proposed Neural-PDR/MFM across four smartphone-holding modes (a) Hand-1, (b) Swing-1, (c) Hand-2, and (d) Swing-2.

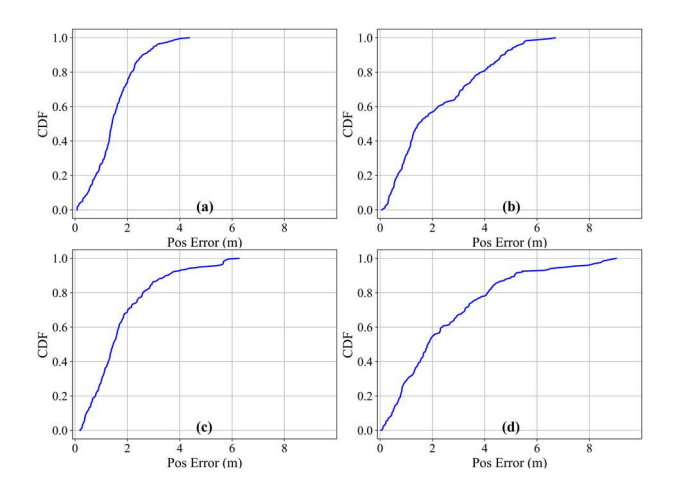


Fig. 13. CDF of reference and Neural-PDR/MFM across four smartphone-holding modes (a) Hand-1, (b) Swing-1, (c) Hand-2, and (d) Swing-2.

of the proposed method across various smartphone-holding modes. The trajectories of four tests of the reference and Neural-PDR/MFM across four smartphone-holding modes are shown in Fig. 12. Fig. 13 presents the corresponding cdf curve for Neural-PDR/MFM. The results indicate that the error is minimal when the phone is held flat. When there are transitions in smartphone modes, the instability of the smartphone's orientation relative to the pedestrian leads to a decline in positioning performance. The error in the swinging state is slightly larger than that in the stable handheld state, yet the positioning accuracy remains sufficient for the positioning needs of pedestrians. Overall, the proposed algorithm demonstrates a strong adaptability to the positioning requirements of pedestrians across various smartphone holding modes.

From the MFM perspective, the main parameters influencing MFM positioning performance include the resolution of the magnetic field map, length, deformation error, and scale error of the MFS. The resolution of the magnetic field map refers to the grid length of the map, which is set to 0.3 m in this article. The deformation error of the MFS primarily refers to the handing drift error of the PDR, while the scale error

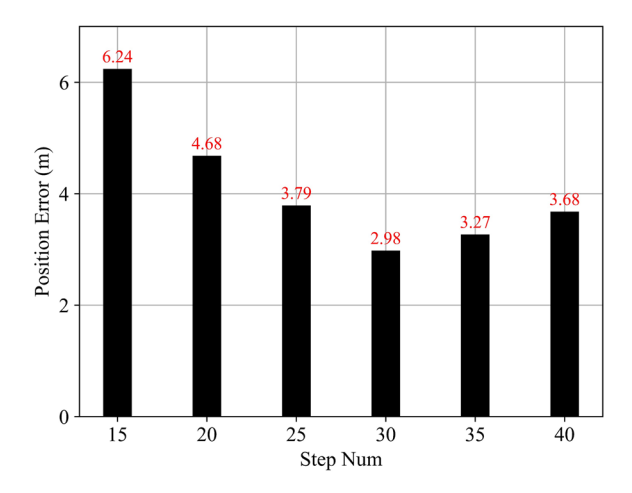


Fig. 14. Mean rms of the position errors of MFM using different lengths of MFS across the 12 tests.

arises from the step length of the PDR. The effects of these three parameters on MFM have been discussed in [37]. While the impact of MFS length has also been examined in [43] for indoor environments, the distinct magnetic characteristics of urban canyons necessitate a dedicated analysis.

To determine a suitable MFS length for this environment, we conducted an ablation study, with results shown in Fig. 14. The figure illustrates the mean rms positioning errors for MFS lengths ranging from 15 to 40 steps across all 12 tests. The positioning error initially decreases and then increases, with the minimum error achieved at a length of 30 steps. This trend has a clear physical interpretation. A short MFS (e.g., 15 steps) lacks sufficient length to capture a unique magnetic signature, leading to ambiguity in matching. Conversely, an excessively long MFS (e.g., 40 steps) is more susceptible to accumulated PDR drift, which distorts the sequence shape and degrades matching accuracy. Furthermore, it may contain redundant information that obscures the primary features.

Therefore, an MFS length of 30 steps (approximately 21 m, assuming an average step length of 0.7 m) was selected, as it strikes an optimal balance between capturing distinctive magnetic features and mitigating the impact of PDR's cumulative errors. This optimal value is derived from our specific test environments and may vary in other urban canyons with different magnetic field characteristics (e.g., different density or scale of anomalies). However, for the scope of this study, our analysis provides a well-reasoned justification for selecting 30 steps as a robust and effective parameter.

Simultaneously, due to the incorporation of deep learning models in this study, the computational complexity is comparatively high. Therefore, it is imperative to discuss whether the computational efficiency of the proposed algorithm fulfills the requirements for pedestrians whose positioning terminals are mobile devices. The computational efficiency of the algorithm was assessed using 12 tests, comparing the average execution times of S-PDR/MFM and Neural-PDR/MFM. The experiment used a computer with a 16-core CPU (11th Gen Intel Core i7-11700 @ 2.50 GHz 16) for processing experimental data. The average duration for each of the 12 tests was 712.62 s,

with an average execution time of 2.087 s for S-PDR/MFM and 5.181 s for Neural-PDR/MFM. The algorithm proposed in this article incurs approximately a twofold increase in time expenditure compared to S-PDR/MFM. However, it still achieves a real-time factor of 137 times (i.e., 712.62/5.181 s).

Mobile devices are less powerful than their desktop counterparts. However, this significant performance margin of 137 times provides a strong buffer, suggesting that the algorithm would maintain real-time capability even on hardware that is an order of magnitude slower. Furthermore, for practical on-device deployment, the model can be significantly optimized using standard industry techniques such as model quantization (e.g., converting weights to 8-bit integers) and deployment via mobile-native inference engines like Tensor-Flow Lite or Core ML, which leverage hardware accelerators (NPUs/GPUs). These optimizations are known to yield dramatic speedups. Therefore, the combination of the large initial performance margin and the potential for established optimization techniques provides compelling evidence that the proposed algorithm is feasible for real-time positioning on contemporary mobile devices.

VII. CONCLUSION AND FUTURE WORK

This article presents a meter-level pedestrian positioning solution integrating INS, LLIO-Net, and MFM, specifically designed for smartphone positioning in urban canyon environments where GNSS signals are severely obstructed and disturbed. The spatial distribution of MFFs in urban canyon environments is analyzed initially, demonstrating sufficient positional resolution for effective positioning. Subsequently, a comprehensive pedestrian positioning algorithm is developed. Considering the diversity of smartphone-holding modes among pedestrians and the presence of staircases in urban canyons, learned inertial odometry is implemented instead of conventional PDR to enhance MFM. Specifically, the positioning accuracy and reliability of MFM are substantially improved by using the relative displacement increments generated by LLIO-Net to produce more precise MFS. Moreover, given the limitations of EKF in processing historical state information, MSCKF is employed to integrate the relative displacement increments and MFM positioning results, thereby establishing a robust pedestrian positioning solution optimized for urban canyon environments. Experimental results demonstrate that the proposed method effectively meets pedestrian positioning requirements in urban canyons, achieving a positioning error of 2.98 m (rms). Compared to the S-PDR/MFM approach, the proposed method exhibits superior adaptability across various application scenarios, demonstrating a substantial improvement in positioning accuracy of 92.22%.

The proposed method effectively addresses the pedestrian positioning requirements in urban canyon environments, demonstrating reliability, cost-effectiveness, and scalability. Nevertheless, certain limitations necessitate further investigation. The method's performance degrades in areas where distinctive magnetic features are either naturally absent or have become outdated due to long-term environmental changes. To address these challenges, future work should focus on two key directions. First, developing adaptive strategies, such as

crowdsourced database maintenance, is crucial for ensuring the long-term validity of the fingerprint map. Second, to enhance overall robustness and continuity, fusing the magnetic field data with other available signals—such as partially available GNSS, Wi-Fi, or visual landmarks—is a promising path. Such a hybrid system would intelligently leverage multiple data sources to ensure reliable positioning across a wider range of conditions.

REFERENCES

- [1] H. Huang, "Location based services," in *Springer Handbook of Geographic Information*. Cham, Switzerland: Springer, 2022, pp. 629–637, doi: 10.1007/978-3-030-53125-6 22.
- [2] G. Retscher, "Pedestrian navigation systems and location-based services," in *Proc. 5th IEE Int. Conf. 3G Mobile Commun. Technol. (3G) Premier Tech. Conf. 3G Beyond*, Oct. 2004, pp. 359–363, doi: 10.1049/ CP:20040696.
- [3] M. A. Cheema, "Indoor location-based services: Challenges and opportunities," SIGSPATIAL Special, vol. 10, no. 2, pp. 10–17, Nov. 2018, doi: 10.1145/3292390.3292394.
- [4] H. Huang, G. Gartner, J. M. Krisp, M. Raubal, and N. Van De Weghe, "Location based services: Ongoing evolution and research agenda," *J. Location Based Services*, vol. 12, no. 2, pp. 63–93, Apr. 2018, doi: 10.1080/17489725.2018.1508763.
- [5] P. Xie and M. G. Petovello, "Measuring GNSS multipath distributions in urban canyon environments," *IEEE Trans. Instrum. Meas.*, vol. 64, no. 2, pp. 366–377, Feb. 2015, doi: 10.1109/TIM.2014.2342452.
- [6] L.-T. Hsu, "Analysis and modeling GPS NLOS effect in highly urbanized area," GPS Solutions, vol. 22, no. 1, p. 7, Nov. 2017, doi: 10.1007/s10291-017-0667-9.
- [7] Y. Patou, S. Obana, and S. Tang, "Improvement of pedestrian positioning precision by using spatial correlation of multipath error," in *Proc. IEEE Int. Conf. Veh. Electron. Saf. (ICVES)*, Sep. 2018, pp. 1–8, doi: 10.1109/ ICVES.2018.8519513.
- [8] L. Benvenuto, T. Cosso, and G. Delzanno, "An adaptive algorithm for multipath mitigation in GNSS positioning with Android smartphones," *Sensors*, vol. 22, no. 15, p. 5790, Aug. 2022, doi: 10.3390/s22155790.
- [9] D. Betaille, F. Peyret, M. Ortiz, S. Miquel, and L. Fontenay, "A new modeling based on urban trenches to improve GNSS positioning quality of service in cities," *IEEE Intell. Transp. Syst. Mag.*, vol. 5, no. 3, pp. 59–70, Fall. 2013, doi: 10.1109/MITS.2013.2263460.
- [10] L.-T. Hsu, Y. Gu, and S. Kamijo, "3D building model-based pedestrian positioning method using GPS/GLONASS/QZSS and its reliability calculation," GPS Solutions, vol. 20, no. 3, pp. 413–428, Jul. 2016, doi: 10.1007/s10291-015-0451-7.
- [11] D. Weng, Z. Hou, Y. Meng, M. Cai, and Y. Chan, "Characterization and mitigation of urban GNSS multipath effects on smartphones," *Measurement*, vol. 223, Dec. 2023, Art. no. 113766, doi: 10.1016/j.measurement.2023.113766.
- [12] D. Weng, W. Chen, S. Ji, and J. Wang, "Intelligent urban positioning using smartphone-based GNSS and pedestrian network," *IEEE Internet Things J.*, vol. 11, no. 12, pp. 22537–22549, Jun. 2024, doi: 10.1109/ JIOT.2024.3381597.
- [13] P. D. Groves, "Shadow matching: A new GNSS positioning technique for urban canyons," *J. Navigat.*, vol. 64, no. 3, pp. 417–430, Jul. 2011, doi: 10.1017/s0373463311000087.
- [14] L. Wang, P. D. Groves, and M. K. Ziebart, "Smartphone shadow matching for better cross-street GNSS positioning in urban environments," J. Navigat., vol. 68, no. 3, pp. 411–433, May 2015, doi: 10.1017/s0373463314000836.
- [15] M. Adjrad and P. D. Groves, "Intelligent urban positioning: Integration of shadow matching with 3D-mapping-aided GNSS ranging," J. Navigat., vol. 71, no. 1, pp. 1–20, Jan. 2018, doi: 10.1017/s0373463317000509.
- [16] H.-F. Ng, G. Zhang, and L.-T. Hsu, "Robust GNSS shadow matching for smartphones in urban canyons," *IEEE Sensors J.*, vol. 21, no. 16, pp. 18307–18317, Aug. 2021, doi: 10.1109/JSEN.2021.3083801.
- [17] Y. Zhao, "Standardization of mobile phone positioning for 3G systems," IEEE Commun. Mag., vol. 40, no. 7, pp. 108–116, Jul. 2002, doi: 10.1109/MCOM.2002.1018015.
- [18] L. Italiano, B. C. Tedeschini, M. Brambilla, and M. Nicoli, "Pedestrian positioning in urban environments with 5G technology," in *Proc.* 22nd Medit. Commun. Comput. Netw. Conf. (MedComNet), Jun. 2024, pp. 1–6, doi: 10.1109/MedComNet62012.2024.10578126.

- [19] Y. Wang, X. Yang, Y. Zhao, Y. Liu, and L. Cuthbert, "Bluetooth positioning using RSSI and triangulation methods," in *Proc. IEEE 10th Consum. Commun. Netw. Conf. (CCNC)*, Jan. 2013, pp. 837–842, doi: 10.1109/CCNC.2013.6488558.
- [20] Z. Huang, L. Xu, and Y. Lin, "Multi-stage pedestrian positioning using filtered WiFi scanner data in an urban road environment," *Sensors*, vol. 20, no. 11, p. 3259, Jun. 2020, doi: 10.3390/s20113259.
- [21] Y. Su, L. Chen, and X. Liu, "Crowdsourced WiFi fingerprint localization in urban canyon," *Int. Arch. Photogramm., Remote Sens. Spatial Inf. Sci.*, vol. 46, pp. 177–184, Apr. 2022, doi: 10.5194/isprs-archives-xlvi-3-w1-2022-177-2022.
- [22] W. Kang and Y. Han, "SmartPDR: Smartphone-based pedestrian dead reckoning for indoor localization," *IEEE Sensors J.*, vol. 15, no. 5, pp. 2906–2916, May 2015, doi: 10.1109/JSEN.2014.2382568.
- [23] N. Roy, H. Wang, and R. Roy Choudhury, "I am a smartphone and I can tell my user's walking direction," in *Proc. 12th Annu. Int. Conf. Mobile Syst., Appl., Services*, Jun. 2014, pp. 329–342, doi: 10.1145/2594368.2594392.
- [24] D. Liu et al., "A novel heading estimation algorithm for pedestrian using a smartphone without attitude constraints," in *Proc. 4th Int. Conf. Ubiquitous Positioning, Indoor Navigat. Location Based Services (UPINLBS)*, Nov. 2016, pp. 29–37, doi: 10.1109/UPINLBS.2016.7809947.
- [25] W. Liu et al., "TLIO: Tight learned inertial odometry," *IEEE Robot. Autom. Lett.*, vol. 5, no. 4, pp. 5653–5660, Oct. 2020, doi: 10.1109/LRA.2020.3007421.
- [26] Y. Wang, J. Kuang, X. Niu, and J. Liu, "LLIO: Lightweight learned inertial odometer," *IEEE Internet Things J.*, vol. 10, no. 3, pp. 2508–2518, Feb. 2023, doi: 10.1109/JIOT.2022.3214087.
- [27] S. Godha and M. E. Cannon, "GPS/MEMS INS integrated system for navigation in urban areas," GPS Solutions, vol. 11, no. 3, pp. 193–203, Jul. 2007, doi: 10.1007/s10291-006-0050-8.
- [28] W. Chen et al., "An integrated GPS and multi-sensor pedestrian positioning system for 3D urban navigation," in *Proc. Joint Urban Remote Sens. Event*, May 2009, pp. 1–6, doi: 10.1109/URS.2009.5137690.
- [29] L.-T. Hsu, Y. Gu, Y. Huang, and S. Kamijo, "Urban pedestrian navigation using smartphone-based dead reckoning and 3-D map-aided GNSS," *IEEE Sensors J.*, vol. 16, no. 5, pp. 1281–1293, Mar. 2016, doi: 10.1109/JSEN.2015.2496621.
- [30] X. Li, D. Wei, W. Zhang, Y. Xu, and H. Yuan, "Integrated PDR/GNSS at different times for pedestrian localization in urban canyon," *IEEE Access*, vol. 9, pp. 22698–22710, 2021, doi: 10.1109/ ACCESS.2021.3055485.
- [31] C. Jiang, Y. Chen, C. Chen, and J. Hyyppä, "Walking gaits aided mobile GNSS for pedestrian navigation in urban areas," *IEEE Internet Things J.*, vol. 11, no. 5, pp. 8499–8510, Mar. 2024, doi: 10.1109/ JIOT.2023.3319014.
- [32] J. Ye, Y. Li, H. Luo, J. Wang, W. Chen, and Q. Zhang, "Hybrid urban canyon pedestrian navigation scheme combined PDR, GNSS and beacon based on smartphone," *Remote Sens.*, vol. 11, no. 18, p. 2174, Sep. 2019, doi: 10.3390/rs11182174.
- [33] H. Luo et al., "Integration of GNSS and BLE technology with inertial sensors for real-time positioning in urban environments," *IEEE Access*, vol. 9, pp. 15744–15763, 2021, doi: 10.1109/ACCESS.2021.3052733.
- [34] J. Kuang, X. Niu, P. Zhang, and X. Chen, "Indoor positioning based on pedestrian dead reckoning and magnetic field matching for smartphones," *Sensors*, vol. 18, no. 12, p. 4142, Nov. 2018, doi: 10.3390/s18124142.
- [35] J. Kuang, T. Li, and X. Niu, "Magnetometer bias insensitive magnetic field matching based on pedestrian dead reckoning for smartphone indoor positioning," *IEEE Sensors J.*, vol. 22, no. 6, pp. 4790–4799, Mar. 2022, doi: 10.1109/JSEN.2021.3073397.
- [36] Y. Wang, J. Kuang, Y. Li, and X. Niu, "Magnetic field-enhanced learning-based inertial odometry for indoor pedestrian," IEEE Trans. Instrum. Meas., vol. 71, pp. 1–13, 2022, doi: 10.1109/ TIM.2022.3186358.
- [37] J. Kuang, T. Li, Q. Chen, B. Zhou, and X. Niu, "Consumer-grade inertial measurement units enhanced indoor magnetic field matching positioning scheme," *IEEE Trans. Instrum. Meas.*, vol. 72, pp. 1–14, 2023, doi: 10.1109/TIM.2022.3221754.
- [38] X. Niu, T. Liu, J. Kuang, and Y. Li, "A novel position and orientation system for pedestrian indoor mobile mapping system," *IEEE Sensors J.*, vol. 21, no. 2, pp. 2104–2114, Jan. 2021, doi: 10.1109/JSEN.2020.3017235.

- [39] H. Touvron et al., "ResMLP: Feedforward networks for image classification with data-efficient training," *IEEE Trans. Pattern Anal. Mach. Intell.*, vol. 45, no. 4, pp. 5314–5321, Apr. 2023, doi: 10.1109/TPAMI.2022.3206148.
- [40] C. Campos, R. Elvira, J. J. G. Rodríguez, J. M. M. Montiel, and J. D. Tardós, "ORB-SLAM3: An accurate open-source library for visual, visual-inertial, and multimap SLAM," *IEEE Trans. Robot.*, vol. 37, no. 6, pp. 1874–1890, Dec. 2021, doi: 10.1109/TRO.2021.3075644.
- [41] S. Chen, J. Kuang, D. Xia, and X. Niu, "Height estimation for floor identification in elevator and escalator scenarios based on smartphones built-in IMU," *IEEE Sensors J.*, vol. 24, no. 19, pp. 29795–29805, Oct. 2024, doi: 10.1109/JSEN.2024.3444918.
- [42] J. Kuang, X. Niu, and X. Chen, "Robust pedestrian dead reckoning based on MEMS-IMU for smartphones," *Sensors*, vol. 18, no. 5, p. 1391, May 2018, doi: 10.3390/s18051391.
- [43] W. Shao et al., "Location fingerprint extraction for magnetic field magnitude based indoor positioning," *J. Sensors*, vol. 2016, pp. 1–16, Jan. 2016, doi: 10.1155/2016/1945695.



Shiyi Chen received the B.Eng. degree in navigation engineering and the M.S. degree in surveying and mapping engineering from Wuhan University, Wuhan, China, in 2023 and 2025, respectively, where he is currently pursuing the Ph.D. degree in geodesy and survey engineering.

His research interests focus on inertial navigation, sensor fusion algorithms, pedestrian navigation, and indoor positioning.



Yan Wang received the B.Eng. degree in chemical engineering and technology and the M.S. degree in computer applied technology from China University of Mining and Technology, Xuzhou, China, in 2016 and 2019, respectively, and the Ph.D. degree from Wuhan University, Wuhan, China, in 2023.

He is currently a Post-Doctoral Research with Wuhan University. His research concentration lies in indoor navigation, sensor fusion algorithms, and computer vision.



Tingwei Wang received the B.Eng. degree in measurement and control technology and instrument and the M.S. degree in navigation engineering from Wuhan University, Wuhan, China, in 2021 and 2024, respectively.

Her research interests focus on inertial navigation, pedestrian navigation, and indoor positioning.



Jian Kuang received the B.Eng. and Ph.D. degrees (Hons.) in geodesy and survey engineering from Wuhan University, Wuhan, China, in 2013 and 2019, respectively.

He is currently an Associate Professor with the GNSS Research Center, Wuhan University. His research interests include magnetic field-based navigation, inertial navigation, pedestrian navigation, and indoor positioning.



Xiaoji Niu (Member, IEEE) received the bachelor and Ph.D. degrees (Hons.) from the Department of Precision Instruments, Tsinghua University, Beijing, China, in 2002 and 1997, respectively.

He is a Professor at GNSS Research Center, Wuhan University, Wuhan, China. He was a Post-Doctoral Research at the University of Calgary, Calgary, AB, Canada, and worked as a Senior Scientist at SiRF Technology Inc., San Jose, CA, USA. He is currently leading the Integrated and Intelligent Navigation (i2Nav) Group, Wuhan University. He

has published 200 + academic papers and owns 50 + patents. His research interests focus on GNSS/INS integration, low-cost navigation sensor fusion, and relevant new applications.